AGU100 ADVANCING EARTH AND SPACE SCIENCE

JGR

Journal of Geophysical Research: Earth Surface

RESEARCH ARTICLE

10.1002/2016JF004138

Key Points:
- The exponent (p) used to model vertical knickpoint recession is similar to the channel concavity (θ)
- The similarity between p and θ hints that the same processes govern waterfall celerity and the incision of nonvertical channel reaches
- The value of p can be biased when the area that drains to waterfalls is similar across a basin and the DEM resolution is low

Supporting Information:
- Supporting Information S1

Correspondence to:
E. Shelef,
shelef@pitt.edu

Citation:
Shelef, E., Haviv, I., & Goren, L. (2018). A potential link between waterfall recession rate and bedrock channel concavity. *Journal of Geophysical Research: Earth Surface*, *123*, 905–923. https://doi.org/10.1002/2016JF004138

Received 7 NOV 2016
Accepted 12 MAR 2018
Accepted article online 22 MAR 2018
Published online 5 MAY 2018

A Potential Link Between Waterfall Recession Rate and Bedrock Channel Concavity

Eitan Shelef[1,2], **Itai Haviv**[2], **and Liran Goren**[2]

[1]Department of Geological and Environmental Science, University of Pittsburgh, Pittsburgh, PA, USA, [2]Department of Geological and Environmental Sciences, Ben-Gurion University of the Negev, Beer Sheva, Israel

Abstract The incision of bedrock channels is typically modeled through the stream power or the shear stress applied on the channel bed. However, this approach is not valid for quasi-vertical knickpoints (hereafter waterfalls), where water and sediments do not apply direct force on the vertical face. As such, waterfall retreat rate is often modeled as a power function of drainage area (a surrogate for hydraulic processes, such as plunge-pool drilling and groundwater seepage, although a variety of non-hydraulic processes may also influence waterfall retreat). These different incision modes are associated with two measurable exponents: the channel concavity, θ, that is measured from the channel topography and is used to evaluate the exponents of drainage area and slope in the channel incision model, and p that is measured from the location of waterfalls within watersheds and evaluates the dependency of the waterfall recession rate on drainage area. To better understand the relations between channel incision and waterfall recession, we systematically compare between the exponents p and θ. These parameters were computed from digital elevation models (30-m Shuttle Radar Topography Mission) of 12 river basins with easily detectable waterfalls. We show that p and θ are (1) similar within uncertainty, (2) come from a similar distribution, and (3) covary for networks with a large number of waterfalls ($\gtrsim 10$). In the context of bedrock incision models this hints that the same processes govern waterfall retreat rate and the incision of nonvertical channel reaches in the analyzed basins and/or that downstream incision can dictate waterfall retreat rate.

1. Introduction

Quantification of landscape response to climatic and tectonic changes is a key component in predicting topographic sensitivity to future changes and in reconstructing past changes from topographic patterns (e.g., Crosby & Whipple, 2006; Goren, 2016; Moon et al., 2011; Whipple & Tucker, 1999). In bedrock landscapes, the rate of channel incision (E [L/T]) is governed by complex interactions between discharge and channel geometry, as well as sediment and bedrock properties (e.g., Dietrich et al., 2003; Gasparini et al., 2006; Seidl & Dietrich, 1992). This rate is often described as a function of gravitationally induced shear stress or stream power applied to the channel bed (e.g., Bagnold, 1966; Howard & Kerby, 1983; Tucker & Hancock, 2010; Whipple & Tucker, 1999) and formulated as follows:

$$E = K A^m S^n, \tag{1}$$

where K [L^{1-2m}/T] is termed the erodibility coefficient and depends on bedrock properties, discharge-drainage area relations, and channel geometry.

In this framework, an increased rate of base-level fall (U [L/T]) is communicated to the upper reaches of the channel network through upstream recession of oversteepend channel segments, namely, knickpoints (e.g., Bishop et al., 2005; Crosby & Whipple, 2006; Rosenbloom & Anderson, 1994; Whipple & Tucker, 1999). When the knickpoint is nonvertical, its recession rate (i.e., knickpoint celerity: C_e [L/T]) can be derived from the channel incision model (equation (1); Berlin & Anderson, 2007; Bishop et al., 2005; Haviv et al., 2006; Rosenbloom & Anderson, 1994; Whipple & Tucker, 1999):

$$C_e = K A^m S^{n-1}. \tag{2}$$

The celerity, C_e, is independent of the slope (S) in two commonly assumed scenarios: (1) when $n = 1$ (Berlin & Anderson, 2007; Rosenbloom & Anderson, 1994), such that $m/n = m$, and (2) when the slope of the knickpoint

is the slope predicted for a steady state landscape under the new rate (U_n) of base-level fall (i.e., $U_n = E$ such that $S = \left(\frac{U_n}{K}\right)^{1/n} A^{-m/n}$ can be substituted into equation (2)). In both cases equation (2) results in

$$C_e \propto A^{m/n}, \tag{3}$$

where in the latter case C_e also depends on U (e.g., Niemann et al., 2001; Wobus, Crosby, & Whipple, 2006).

When U and K are generally uniform along the channel, the ratio m/n equals the channel concavity index, θ, that is typically computed from linear relations between log(S) and log(A) or between topographic elevation, z, and a transformation variable, χ, (Mudd et al., 2014; Perron & Royden, 2012). In that case, equation (3) becomes the following:

$$C_e \propto A^{\theta}. \tag{4}$$

When a knickpoint is quasi-vertical (i.e., a waterfall) such that water and sediment fall without applying direct force on the knickpoint face, the assumptions that underly equations (1) and (2) become invalid (Crosby & Whipple, 2006; Haviv et al., 2010). In that case, waterfall recession is influenced by a variety of processes, including plunge pool drilling, freeze-thaw and wet-dry cycles, and groundwater seepage. The intensity of these processes depends on factors such as cap rock and sub–cap rock strength and joint density, sediment concentration and grain-size distribution, water discharge, the microtopography of the waterfall lip, the waterfall height, temperature and rainfall fluctuations, water jet impact angle, and the properties of the lag debris (e.g., Gilbert, 1907; Haviv et al., 2006, 2010; Howard & Kochel, 1988; Lamb et al., 2007, 2014; Mackey et al., 2014; Mason & Arumugam, 1985; Scheingross et al., 2017). Whereas this suggests that multiple factors should be parameterized to accurately model waterfall celerity (e.g., Haviv et al., 2010; Lamb et al., 2006; Scheingross & Lamb, 2016), a simple model for waterfall celerity (C_{ew} [L/T]) was posited by Crosby and Whipple (2006) and explored in various settings (Berlin & Anderson, 2007; Brocard et al., 2016; Crosby & Whipple, 2006; DiBiase et al., 2015; Haviv, 2007; Mackey et al., 2014):

$$C_{ew} = B A^{p}, \tag{5}$$

where B [L^{1-2p}/T] is a proportionality constant and p is a positive exponent. In this model both B and p are not necessarily related to an incision model such as the one presented in equation (1).

The different geometry of waterfalls and nonvertical knickpoints suggests that their recession rate might be governed by different processes, where the recession of nonvertical knickpoints is often formulated based on the bedrock channel incision model (equation (2)), and that of waterfalls (i.e., equation (5)) is based on empirically demonstrated relations with drainage area (e.g., Berlin & Anderson, 2007; Crosby & Whipple, 2006). However, the similarity in the functional form of equations (4) and (5) suggests a potential link between the two rates and highlights the need for a systematic comparison between θ and p. Such a comparison can shed light on commonalities and/or differences between the two rates and the underlying processes. Published data indicate that θ values typically vary between 0.35 and 0.7 (Tucker & Whipple, 2002; Whipple & Tucker, 1999), whereas p values span a wider range ($p = -3$, 0, 0.24,0.33, 0.54, and 1.125 for Berlin & Anderson, 2007; Crosby & Whipple, 2006; DiBiase et al., 2015; Haviv, 2007; Mackey et al., 2014; Weissel & Seidl, 1998; respectively). These published data, however, are hindered by the small number of reported p measurements and the general lack of uncertainty bounds for reported p and θ values. Further, p and θ values are often not measured over the same channel segments and, as far as we know, the covariance between them has not been explored.

In this study we compare p and θ over the same channel sections while quantifying their uncertainty. We also explore the covariance between p and θ and the influence of various factors on p. To do so, we use existing and new methods to compute p, θ, and their uncertainty from digital elevation models (DEMs) of 12 river basins with multiple waterfalls. Our analyses indicate that p and θ are (1) similar within uncertainty, (2) come from a similar distribution, and (3) generally covary. We also show that optimized p values are sensitive to the variability in the basin area that drains to waterfalls, which could explain the wide range of p values that has been reported in the literature.

Table 1
Properties of the Analyzed Basins

Basin ID	Basin name	Location	Latitude	Longitude	MAP (mm/year)	Lithology	Studies of p in this basin
a	Happy Canyon	Utah, United States	38.137	−110.369	200	Triasic sedimentary rocks (Chinle, Wingate, and Kayenta Formations), primarily mudstone, sandstone, and limestone (1)	—
b	Mineral Canyon	Utah, United States	38.531	−109.976	200	Triasic sedimentary rocks (Chinle, Wingate, and Kayenta Formations), primarily mudstone, sandstone, and limestone (1)	—
c	Taylor Canyon	Utah, United States	38.475	−109.941	250	Triasic sedimentary rocks (Chinle, Wingate, and Kayenta Formations), primarily mudstone, sandstone, and limestone (1)	—
d	Rio Napo	Pastaza, Equador	−1.236	−77.709	4150	Tertiary sedimentary rocks (Arajuno formations), primarily conglomerate, and sandstone (2)	—
e	Chandler River	New South Wales, Australia	−30.708	152.043	1150	Paleozoic metasedimentary rocks (Myra beds and undivided units), primarily schist, slate, phyllite, greywacke, and mudstone (3)	Weissel and Seidl (1998) Weissel and Seidl (1997) Seidl et al. (1996)
f	Macleay River	New South Wales, Australia	−30.783	151.953	950	Paleozoic metasedimentary rocks (Myra beds and undivided units), primarily schist, slate, phyllite, greywacke, and mudstone (3)	Weissel and Seidl (1998) Weissel and Seidl (1997) Seidl et al. (1996)
g	Apsley River	New South Wales, Australia	−30.884	152.028	1150	Paleozoic metasedimentary rocks (Myra beds and undivided units), primarily schist, slate, phyllite, greywacke, and mudstone (3)	Weissel and Seidl (1998) Weissel and Seidl (1997) Seidl et al. (1996)
h	Parachute Creek	Colorado, United States	39.467	−108.076	400	Tertiary sedimentary rocks (Wasatch and Green River Formations), primarily shale, sandstone, and marlstone (4)	Berlin and Anderson (2007)
i	Roan Creek	Colorado, United States	39.406	−108.269	400	Tertiary sedimentary rocks (Wasatch and Green River Formations), primarily shale, sandstone, and marlstone (4)	Berlin and Anderson (2007)
j	Havasu Creek	Arizona, United States	36.272	−112.719	300	Permian sedimentary rocks (Kaibab, Toroweap, Coconino, and Hermit Formations), primarily limestone, shale, and sandstone (5)	—
k	Tuckup Canyon	Arizona, United States	36.298	−112.876	300	Permian sedimentary rocks (Kaibab, Toroweap, Coconino, Hermit Formations), primarily limestone, shale, and sandstone (5)	—
l	Surprise Canyon	Arizona, United States	35.925	−113.610	250	Permian sedimentary rocks (Kaibab, Toroweap, Coconino, and Hermit Formations), primarily limestone, shale, and sandstone (5)	—

Note. The lithologic data is from the following sources: (1) http://files.geology.utah.gov/online/usgs/; (2) Ruiz (2002); (3) http://www.resourcesandenergy.nsw.gov.au; (4) Berlin and Anderson (2007) and Hail (1992); and (5) http://pubs.usgs.gov/imap/. Basin IDs Are Identical to Those in Figure 1, Latitude and Longitude (Decimal Degrees) Show the Trunk Channel Location, MAP Is the Mean Annual Precipitation (Rounded to the Nearest 50 mm/year Multiplier) Computed From 0.5° Data Set From Precipitation Data Collected Between 1901 and 1914 and Attained From https://crudata.uea.ac.uk/cru/data/hrg/.

2. Method

To explore the similarity between p and θ, we analyze 12 natural basins with multiple waterfalls in different climatic and lithologic conditions (Tables 1 and S1 in the supporting information). We first detect the location of waterfalls and the uncertainty in their location in a systematic manner (section 2.2). We then use these locations and uncertainties to compute the optimal p and θ values (sections 2.3 and 2.4), and their uncertainty (section 2.5) for each of the analyzed basins. For consistency, we compute the values of θ over

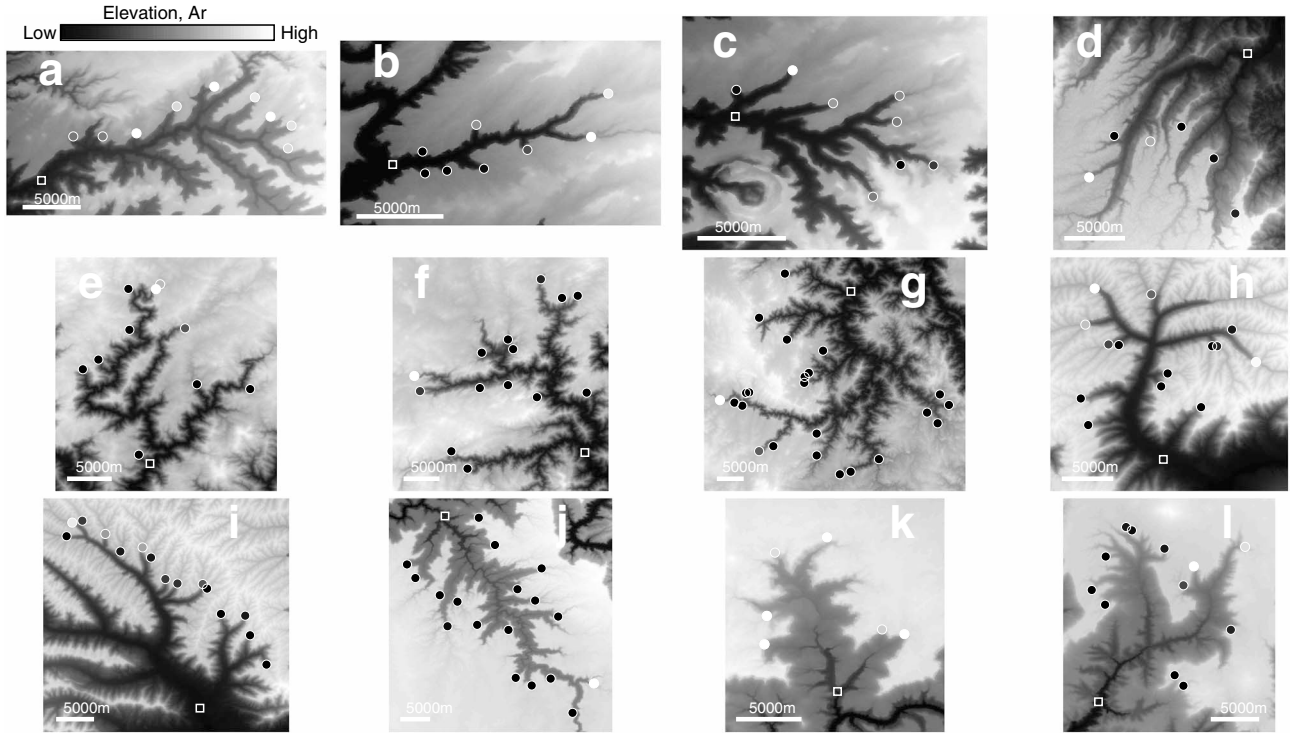

Figure 1. Digital elevation models of the 12 basins analyzed in this study. Panels are labeled in accordance with the basin ID in Tables 1 and S1, where more information is provided regarding the location and characteristics of the different basins. Maps are oriented with north upward and lighter colors represent higher elevation. Circles show the location of waterfalls, and a white square shows the prescribed location of the initial waterfall for each basin. Circles are colored by drainage area relative to the mean value (μ_a) for all waterfalls in the basin ($A_r = \frac{A_w}{(\mu_a)}$, where light colors indicate A_r values that are relatively high for each basin, and A_w is the drainage area at the waterfall) to illustrate the scatter in drainage area at waterfalls. Note that waterfalls in basins (a) and (k) have lower variation in A_r values compared to other basins where some waterfalls are associated with very high A_r values (light color), while others with very low (dark color). The colorbar pertains to both elevation and A_r. Basin locations are (a–c) Utah, United States, (d) Pastaza, Equador, (e–g) New South Wales, Australia, (h and i) Colorado, United States, and (j–l) Arizona, United States.

the same channel sections used to compute p (i.e., between the waterfalls and a downstream location that drains all waterfalls). To verify that our results are consistent across methods for p and θ computation, we use three different methods to compute θ and two methods to compute p. The resulting p and θ values are then compared.

2.1. Study Sites

We explored the values of p and θ by analyzing basins with multiple waterfalls identified using a 1-arc second Shuttle Radar Topography Mission DEM (~30 m for the studied basins; Rodríguez et al., 2005; Tables 1 and S1). The basins were selected based on the following criteria: (1) multiple waterfalls (to effectively constrain p), (2) waterfalls are clearly detectable over the DEM resolution (section 2.2 and Figure 1), (3) the drainage area at the waterfall (A_w) in some of the selected basins spans a wide range of values such that in these cases it is unlikely that waterfall location can be explained solely via a drainage area threshold (i.e., Crosby & Whipple, 2006), and (4) basins span different precipitation regimes in order to explore the potential influence of precipitation on p and θ (e.g., Zaprowski et al., 2005; Table 1).

2.2. Waterfall Identification

We applied a quasi-automatic waterfall identification procedure to detect waterfalls in a repeatable and efficient manner (Figure 2). We first used the DEM to visually detect all potential waterfalls within a basin and extract the profiles of channel segments that contain waterfalls. For each segment we identified the waterfall location and its boundaries using the following procedure, (a) for each node along the channel segment we recorded elevation and drainage area (z_i, A_i, where i is the node index); (b) the slope (S_i) at each node was computed via a central difference scheme over a window of nine nodes (a window size selected based on iterative experimentation) along the channel to suppress slope errors that propagate from elevation errors in the DEM (i.e., Wobus, Whipple, et al., 2006); (c) values of k_{sn} (normalized channel steepness index, (e.g., Wobus, Whipple, et al., 2006)) were computed for each channel node utilizing $k_{sn_i} = S_i A_i^{0.5}$ (an exponent

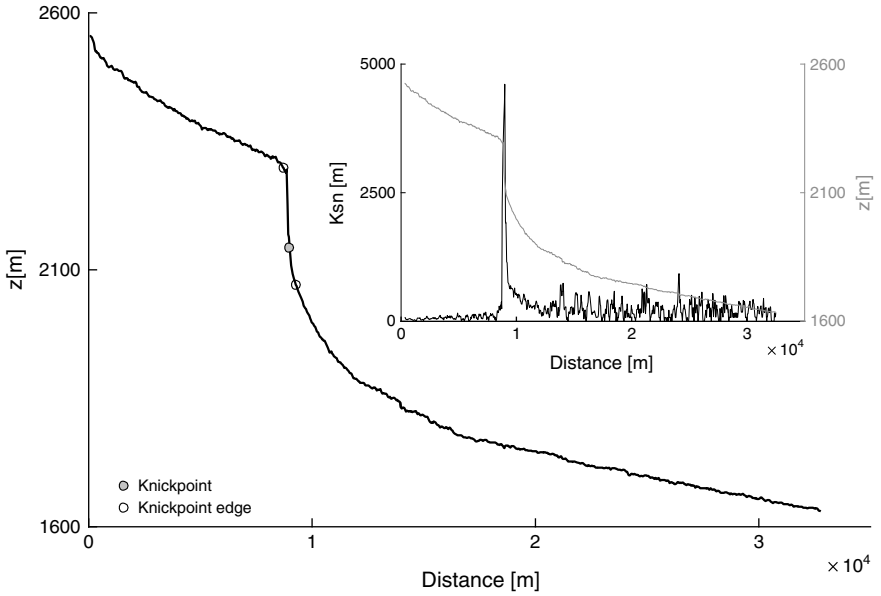

Figure 2. An example for quasi-automatic knickpoint detection. The main figure shows the profile of a channel in basin (I) in Figure 1 and the location of the detected knickpoint (filled circle) and its top and bottom boundaries (open circles). The inset graph shows the same profile (gray line, right *y* axis) and the associated k_{sn} values (black line, left *y* axis).

value of 0.5 is generally similar to that computed for most basins we studied, and is in agreement with values that are traditionally used); (d) waterfall location was detected by finding the node of highest k_{sn_i}, where the slope across the waterfall also exceeds a prescribed threshold (0.2, in agreement with the upper slope limit of step pool and cascade reaches (Montgomery & Buffington, 1997; Montgomery et al., 1995) as well as lag debris reaches beneath waterfalls (Haviv, 2007; Haviv et al., 2010)); (e) the top and bottom boundaries of the waterfall were defined by progressing from the waterfall upstream and downstream until the first node, where S_i is smaller than half of the prescribed knickpoint threshold (i.e., < 0.1). If S_i does not decrease below this value, the channel is relatively steep so the waterfall is defined as not being sufficiently distinguishable and is excluded from the analysis. These boundaries are used as measures of uncertainty in waterfall location. We executed this routine over all basins and visually confirmed the location of the selected waterfalls and their boundaries (Figure 3).

2.3. Computation of *p* Value

2.3.1. Time-Based Optimization of *p*

To compute *p* for each basin, we used an optimization procedure that minimizes the scatter in recession duration (i.e., the time span of recession) among the observed waterfalls (e.g., Brocard et al., 2016). This procedure relies on a commonly used assumption (e.g., Berlin & Anderson, 2007; Brocard et al., 2016; Crosby & Whipple, 2006; Weissel & Seidl, 1998) that all waterfalls initiated as a single waterfall that was located at the trunk channel at some initial time t_s, and over the time period between t_s and the present (hereafter recession duration) receded and bifurcated at tributary junctions to their current location. We also assume that the waterfall recession rate is described by equation (5) and that the value of *B* and *p* are uniform within the basin. These assumptions are similar to those used by other studies (Berlin & Anderson, 2007; Brocard et al., 2016; Crosby & Whipple, 2006; DiBiase et al., 2015; Whittaker & Boulton, 2012).

The *p* value that optimizes the fit between modeled and natural waterfall locations can be computed either from the spatial misfit between the location of modeled and observed waterfalls (e.g., Berlin & Anderson, 2007; Crosby & Whipple, 2006) or from the temporal misfit in arrival time of the modeled waterfall to the location of the observed ones (e.g., Brocard et al., 2016). We computed *p* through the latter approach that is most consistent with the assumption that all waterfalls migrated to their current position over the same time period. The recession duration (i.e., the time span of recession) between the initial waterfall location and the current one is cast as (following Berlin & Anderson, 2007; Crosby & Whipple, 2006):

$$t_r(N_n) = \sum_{i=1}^{N_n} \Delta t_i = \sum_{i=1}^{N_n} \frac{\Delta x}{C_{ew,i}} \delta_i, \tag{6}$$

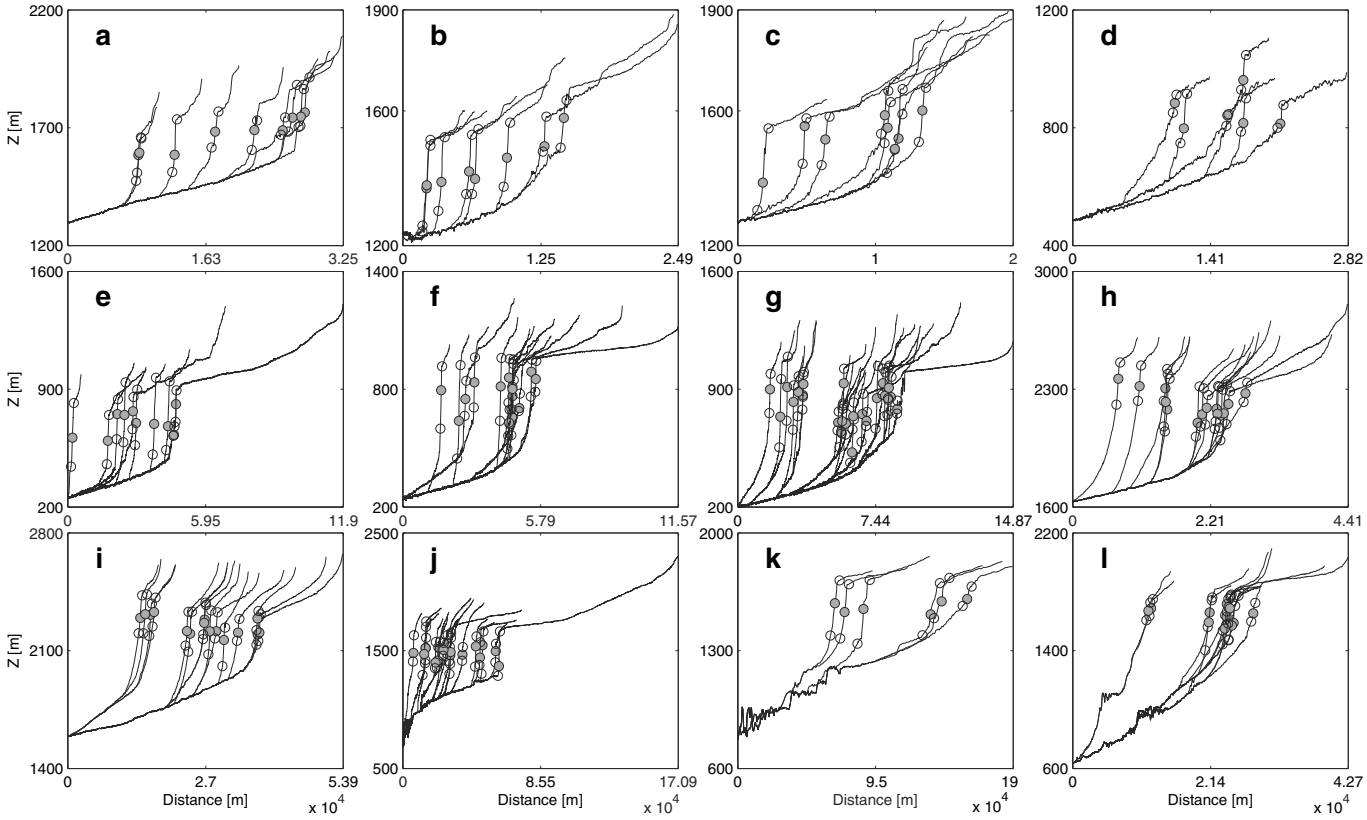

Figure 3. Topographic profiles along the analyzed channel systems. Each panel shows the profiles and the waterfalls for each basin and is labeled in accordance with the basin ID in Table 1. Dark and light colored circles mark the waterfalls and their boundaries, respectively. The lowest extent of the profiles is the prescribed location of the initial knickpoint. The jagged topography of some of the channels reflects the noisy digital elevation model data (this plot shows the raw digital elevation model data rather than a smoothed or pit-filled elevation data).

where N_n is the number of nodes between the initial waterfall location at t_s and the current waterfall location and Δt_i [T] is the recession duration between nodes i and $i+1$. $C_{ew,i}$ [L/T] is the waterfall celerity between nodes i and $i+1$ that is evaluated as $B A_i^p$ (equation (5)), where A_i is the drainage area of the ith node. Δx is the distance between DEM nodes in the cardinal directions, and δ_i is a dimensionless variable that equals 1 or $\sqrt{2}$ for cardinal and diagonal flow direction between nodes i and $i+1$, respectively.

To compute p in cases where the recession duration and initial waterfall location are unknown, we nondimensionalized the duration of waterfall recession to $t_r^*(N_n) = \sum_{i=1}^{N_n} \Delta t_i^*$, where $\Delta t_i^* = \Delta t_i / \Delta t_0$. We set $\Delta t_0 = \frac{\Delta x}{B A_0^p}$, where A_0 is an arbitrary reference drainage area. The nondimensional recession duration is as follows:

$$t_r(N_n)^* = \sum_{i=1}^{N_n} \Delta t_i^* = A_0^p \sum_{i=1}^{N_n} A_i^{-p} \delta_i. \tag{7}$$

We find the optimal p value while accounting for the uncertainty in waterfall positions. To do so, we computed the dimensionless recession duration (t_r^*, equation (7)) between the initial waterfall location and each of the observed waterfalls for each p value (from 0 to 2 in intervals of 0.01). We then calculated the weighted misfit (χ_r^2) in recession duration between waterfalls:

$$\chi_r^2 = \frac{1}{N_p - 1} \sum_{i=1}^{N_p} \frac{D_i^2}{\sigma_i^2} = \frac{1}{N_p - 1} \sum_{i=1}^{N_p} \frac{t_{r,i}^* - \bar{t}_r^*}{\sigma_i^2}, \tag{8}$$

where N_p is the number of waterfalls, D_i is the difference in t_r^* between the ith waterfall ($t_{r,i}^*$) and the mean t_r^* for all waterfalls ($\bar{t}_r^*$), and σ_i is a measure of uncertainty in recession duration computed from the standard deviation of the nondimensional recession time to the top and bottom boundaries of the ith waterfall (because this is a standard deviation of two values only, it equals half of the difference in t_r^* between these

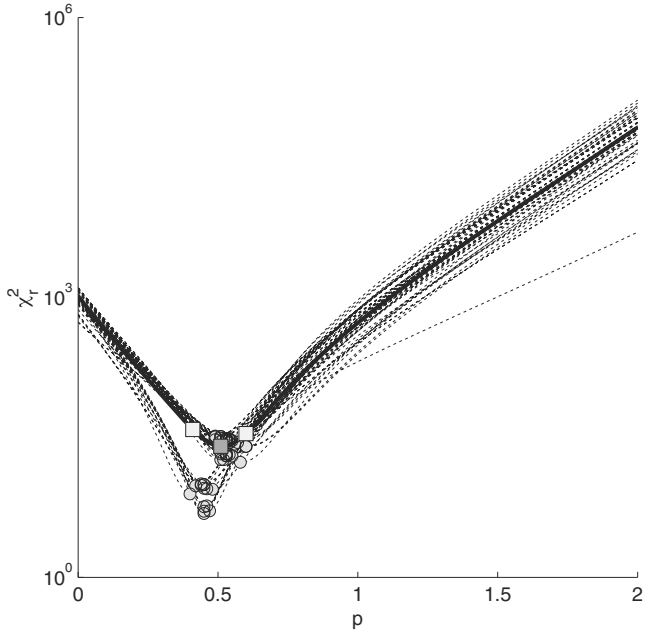

Figure 4. Optimization of p and its associated uncertainty. The χ_r^2 (y axis) versus different p values (x axis) for one of the analyzed basins (basin h, Table 1). The solid line is an optimization curve based on all waterfalls, and the dark gray square marks the optimal p value that minimizes χ_r^2 for this case. Dashed lines show 50 optimization curves for arbitrarily chosen subsets of 75% of all waterfalls, and gray circles mark the optimal p value for each of these iterations. Light squares mark the uncertainty in the optimal p value for all waterfalls, where this uncertainty is determined from the 2.5th and 97.5th percentiles of the optimal p values for the 50 subsets of waterfalls (i.e., the gray circles).

top and bottom boundaries). The best fit p value is the one that produces the lowest χ_r^2 value (Figure 4). The method successfully recovered the correct p values from synthetic experiments where waterfall locations were modeled with a prescribed p values.

As long as the initial location of the waterfall is at the trunk stream downstream of all waterfalls, the optimization of p is insensitive to the exact initial location of the waterfall and the duration of waterfall recession. This is because waterfall recession along a trunk channel downstream of all waterfalls shifts $t_r^*(N_n)$ by a constant value for all waterfalls. Hence, the initial location of the waterfall can be prescribed at any arbitrary location in the trunk channel without affecting the optimization results that rely on minimizing the scatter in $t_r^*(N_n)$ between all waterfalls. This facilitates finding the best fit p without knowing the recession duration and the exact initial location of the waterfall.

The method described above differs from the time-based optimization of Brocard et al. (2016) in that it is designed to compute p while accounting for the uncertainty in waterfall location. To explore whether the p values produced by the time-based approach we used is similar to that produced by the distance-based approach of Crosby and Whipple (2006) and Berlin and Anderson (2007), we also developed a distance-based optimization procedure that can recover p when both the duration of recession and the exact initial location of the waterfalls are unknown. The p values produced by these two approaches are equal within error (see the supporting information).

2.3.2. Optimization of p With a Critical Area Threshold

To account for the possibility that waterfall recession is halted when the basin area that drains to the waterfall is below a critical threshold (A_c [L^2], Crosby & Whipple, 2006), we also computed the optimal p for

$$C_{ew} = B(A - A_c)^p \ . \tag{9}$$

Under these conditions $C_{ew} = 0$ when $A_c \geq A$. The A_c value for each basin was determined as the minimum drainage area over all the waterfalls in the basin. The optimal p value is found by minimizing χ_r^2 as explained in section 2.3 (equation (8)).

2.4. Extraction of θ Value

We computed θ, and the uncertainty associated with it, using slope area (S-A) (e.g., Hack, 1973; Whipple & Tucker, 1999; Wobus, Whipple, et al., 2006) and χ-z (e.g., Perron & Royden, 2012; Royden et al., 2000) relations. For the latter we computed θ for both linear and nonlinear χ-z relations. The analysis is conducted on channel portions that extend from the bottom boundary of waterfalls (i.e., section 2.2) downstream to the mutual junction where the initial waterfall is prescribed. Focusing on these channel portions assures that p and θ are computed and compared over the same set of flow pathways.

2.4.1. Compute θ From Slope Area Relations

The value of θ is reported as the slope of the least square linear regression between log(S) and log(A) (e.g., Dietrich et al., 2003; Howard & Kerby, 1983; Whipple & Tucker, 1999; Wobus, Whipple, et al., 2006) at the relevant channel portions. To reduce the influence of the DEM elevation error on S (i.e., Wobus, Whipple, et al., 2006), we computed S over vertical increments of $\Delta z \simeq 100$ m such that $\frac{\Sigma_z}{\Delta_z} \simeq 0.1$ (where $\Sigma_z = 10$ m, is the 90% DEM elevation error; Rodríguez et al., 2005).

2.4.2. Compute θ From χ-z Relations

An alternate procedure for calculating θ relies on a comparison between elevation (z) and an integral quantity of drainage area (χ [L]) (Goren et al., 2014; Mudd et al., 2014; Perron & Royden, 2012; Royden et al., 2000; Royden & Perron, 2013; Willett et al., 2014):

$$\chi(l) = A_0^\theta \int_{l_b}^{l} A(l)^{-\theta} \mathrm{d}l, \tag{10}$$

where A_0 is a reference A value (we prescribed $A_0 = 1,000\ m^2$) and l and l_b measure the distance along the stream at up and downstream locations, respectively.

In theory, a linear relation between χ and z should occur when all the following conditions are met (Perron & Royden, 2012): (a) the channel network is at steady state, (b) the channel steepness index ($k_s = (U/K)^{1/n}$) is spatially uniform, and (c) θ is spatially uniform, and (d) the channel incision processes are adequately described by equation (1). When these assumptions hold, the integration of channel slope over the distance $l - l_b$ along the channel yields (Perron & Royden, 2012; Shelef & Hilley, 2014; Willett et al., 2014)

$$\begin{aligned} z(l) &= z(l_b) + \int_{l_b}^{l} S(l)\mathrm{d}l, \\ &= z(l_b) + k_s \int_{l_b}^{l} A^{-\theta}\mathrm{d}l, \\ &= z(l_b) + k_s A_0^{-\theta} \chi(l), \end{aligned} \tag{11}$$

where $z(l_b)$ is the z value at $\chi = 0$. Equation (11) demonstrates that when χ is calculated with a θ value that is representative of the analyzed channel and under the above assumptions, the relation between $\chi(l)$ and $z(l)$ is linear and $k_s A_0^{-\theta}$ is the coefficient of proportionality. This equation also implies that when χ is computed for multiple tributaries and is integrated in the upflow direction from a common point downstream, the correct θ value should not only linearize all the profiles in χ-z space but also collapse all tributaries to a single line (Perron & Royden, 2012).

If the channels downstream of waterfalls are assumed to be at steady state, an optimal θ can be identified through an iterative search for a value that minimizes the deviation from a least squares linear regression between χ and z (Mudd et al., 2014; Perron & Royden, 2012; Royden & Perron, 2013) downstream of waterfalls. We used a range of θ values (from 0 to 2 in intervals of 0.01) to compute χ for each DEM node along tributaries that extend from the prescribed initial waterfall location to the bottom of waterfalls. We integrated χ using the rectangle rule to better capture the discrete changes in χ across channel junction (Mudd et al., 2014). For each θ value, we computed the least squares linear regression between χ and z and calculated the misfit between the data and the linear model using equation (8), where D_i is the difference between the observed and predicted elevation at the ith node, σ_i is the DEM vertical error (i.e., 10 m), and N_p is the number of χ-z pairs. The optimal θ value minimizes the misfit equation (8).

Nonlinear χ-z relations may occur when temporally and/or spatially varying uplift, climate, and rock properties affect the geometry of the channel network (e.g., Goren et al., 2014; Mudd et al., 2014; Royden & Perron, 2013). To acknowledge this possibility, we computed θ through a binning approach (after Goren et al., 2014) that minimizes the scatter of z values within each χ bin with multiple tributaries, so that it does not force the same linear relation over the entire χ and z range. For each θ value, the procedure divides the range of χ values to 100 bins (based on an iterative experiment that shows that stable θ values are attained with more than 20 bins) and computes equation (8) for bins that contain more than one tributary. The optimal θ value is that which minimizes equation (8), where D_i is the standard deviation of z values within each bin and σ_i is the DEM vertical error (i.e., 10 m).

2.5. Uncertainty in p and θ

The values of p and θ are often reported without a measure of uncertainty, thus inhibiting a comparison that accounts for the uncertainty in each of these parameters. For θ values computed from the slope of the least squares linear regression of $\log(S)$ versus $\log(A)$ (section 2.4.1), the uncertainty in θ for each of the basins is reported as two standard deviations of the computed slope (Montgomery & Runger, 2010). For θ values computed from χ-z relations (section 2.4.2), as well as for p values computed from t_r^* (section 2.3), we calculated the uncertainty for each basin through an iterative bootstrap approach that repeatedly computes p (or θ) for subsets of the flow pathways in each basin. This is executed for 50 iterations, where in each iteration we compute the optimal p (or θ) value for an arbitrarily chosen subset of the flow pathways (Figure 4). We then compute the lower and upper uncertainty bounds in p (or θ) for each basin from the 2.5th and 97.5th percentiles of the optimal p (or θ) values computed in these 50 iterations (Figure 4). In each iteration the number of flow pathways is the integer value closest to 75% of the total number of flow pathways.

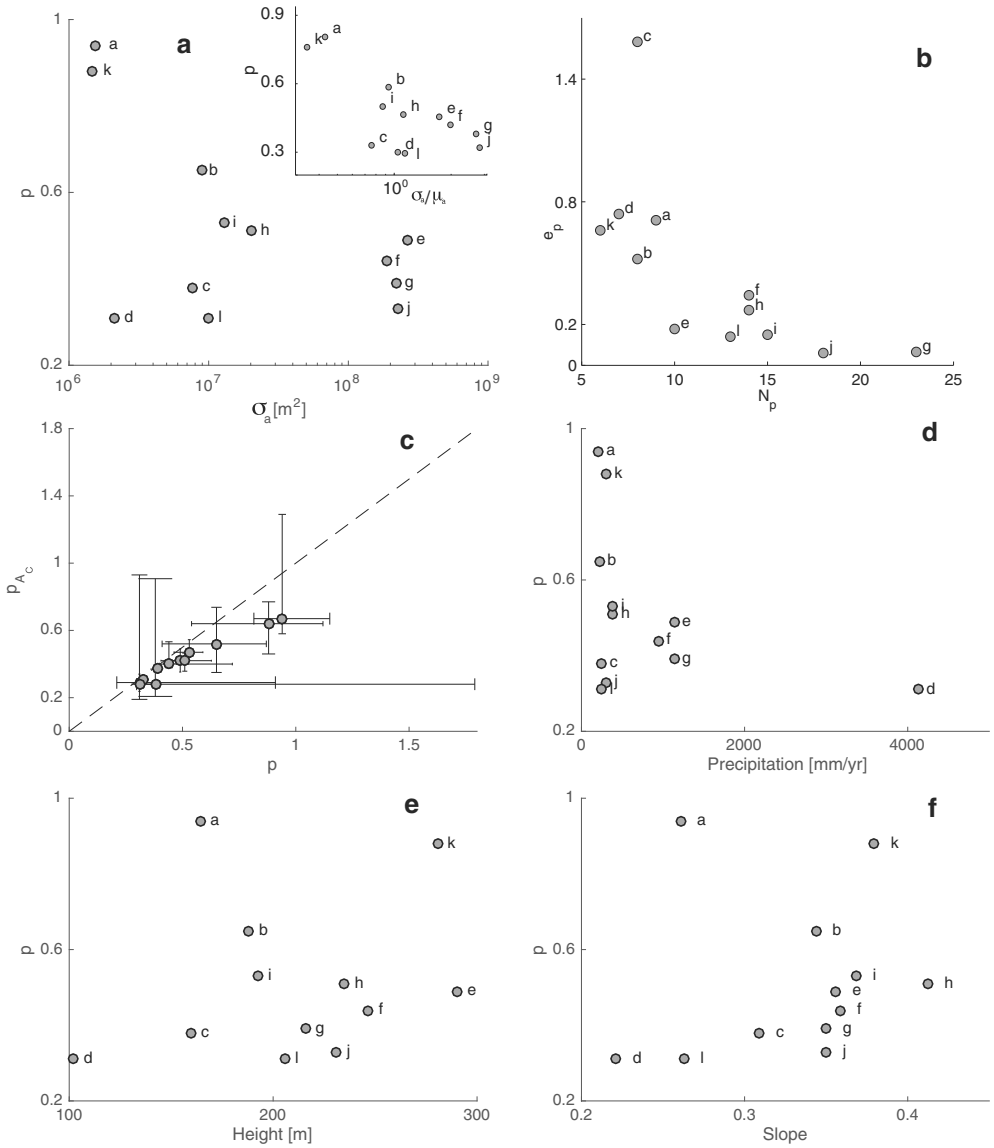

Figure 5. Basin parameters and their influence on p. (a) p values (y axis) versus the standard deviation of drainage area at the waterfalls (σ_a). The inset shows the relative standard deviation σ_a/μ_a, where μ_a is the mean drainage area of waterfalls in the basin (A_w). (b) Uncertainty in p (e_p; the difference between the highest and lowest uncertainty bounds of p from models with and without a critical area threshold [y axis]) versus the number of waterfalls within a basin (x axis). (c) Comparison of p value with $A_c > 0$ (y axis) and $A_c = 0$ (x axis), where A_c is a critical area threshold for waterfall recession. Dashed line shows a 1:1 relation and error bars mark the 95% confidence (see section 2.5). (d) p value (y axis) versus precipitation. (e) p value (y axis) versus mean waterfall height within the basin. (f) p value (y axis) versus mean value of slope between the top and bottom boundaries of all waterfalls within each basin. The p value in plots (d)–(f) are the p values computed with $A_c = 0$. Letters for each data point correspond with basin IDs (Table 1).

3. Results

3.1. Waterfalls, Longitudinal Profiles, and Their Characteristics

Figure 3 shows river longitudinal profiles along the analyzed basins. We find that the elevation of the waterfalls in each basin is generally similar within uncertainty (i.e., the top and bottom boundaries of the waterfall, Figure 3). In some basins this elevation consistently changes with distance from the origin (e.g., Figures 3a–3c and 3h) or is rather scattered (Figure 3f). Review of geologic maps (Table 1), air photos, pictures (https://www.google.com/earth/, http://www.panoramio.com), and previous work (Berlin & Anderson, 2007; Melis et al., 1996; Ruiz, 2002; Weissel & Seidl, 1997, 1998) suggests that in most of the analyzed basins the waterfalls occur over an erosion-resistant sedimentary layer.

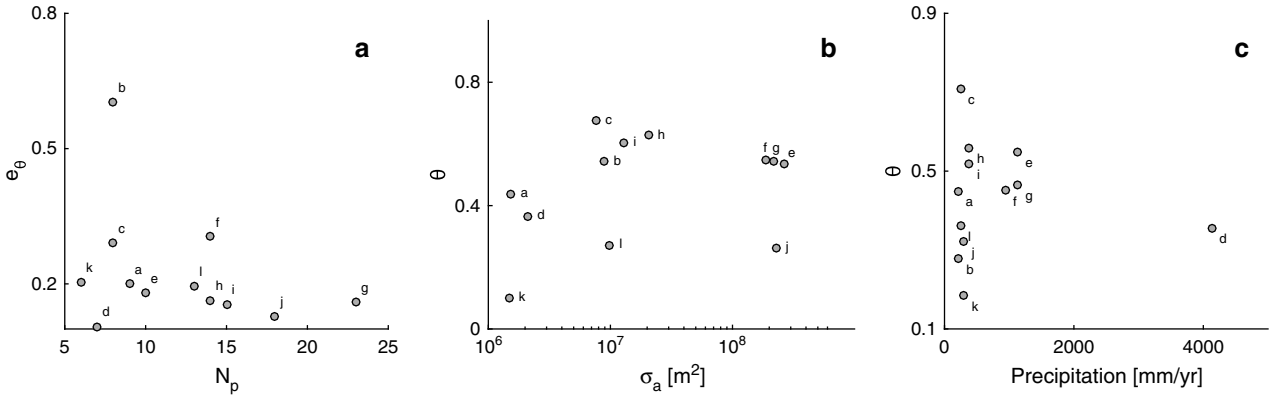

Figure 6. (a) The uncertainty in θ (e_θ; the difference between the highest and lowest uncertainty bounds of the three methods used to compute θ, y axis) versus the number of waterfalls; (b) θ (y axis) versus the standard deviation (σ_a) of drainage area for all waterfalls within a basin. (A_w); and (c) θ (y axis) versus precipitation. Letters for each data point correspond with basin IDs (Table 1).

3.2. Computed *p* Values

Computed values of p typically span a range of 0.3–0.9 (Figure 5 and Table S1). High values of p ($\approx$1) occur in basins (a) and (k) and are associated with a low standard deviation (σ_a) and relative standard deviation (σ_a/μ_a, where μ_a is the mean drainage area at waterfalls) of the drainage area at waterfalls (Figure 5a). The uncertainty in p is sensitive to the number of waterfalls (N_p) in the analyzed basin and suggests that this uncertainty stabilizes when $N_p \gtrsim 10$ (Figure 5b). Values of p computed through the time-based method with and without a critical area threshold (A_c) covary and are similar within uncertainty (Figure 5c), where a model with $A_c > 0$ typically produces lower p values compared to a model with $A_c = 0$. Values of p do not display a clear covariance with precipitation, waterfall height, or slope (Figures 5d–5f, height and slope are measured between the top and bottom waterfall boundaries). The χ_r^2 optimization curves (SI) tend to be better constrained for basins with large number of waterfalls (Table S1 and Figure S2). The p value we computed for basins (e)–(j) ($0.49^{+0.04}_{-0.05}$, $0.44^{+0.28}_{-0.04}$, $0.39^{+0.02}_{-0.03}$, respectively, computed with $A_c = 0$) differs from the p value estimated by Weissel and Seidl (1998) for the same catchment ($p \sim 0$). This deviation likely reflects differences in the DEM resolution, number of waterfalls, and optimization technique. This study uses DEMs of 30-m resolution, 47 waterfalls, and the aforementioned p optimization technique, whereas the study of Weissel and Seidl (1998) used DEMs of 500-m resolution, 11 waterfalls, and visual approximation of p. Further, this study analyzed each basin separately, whereas Weissel and Seidl (1998) analyzed basins (e)–(g) together, starting approximately 150-km downstream of the confluence where these basins join. The p values computed for basins (h) and (i), ($0.51^{+0.12}_{-0.1}$, $0.53^{+0.06}_{-0.07}$, respectively, computed with $A_c = 0$) are similar to the value computed by Berlin and Anderson (2007) for these two basins combined using a distance-based optimization ($p = 0.54$).

3.3. Computed θ Values

Computed values of channel concavity (θ) typically span a range of 0.3–0.7 (Figure 6 and Table S1). In contrast to p, the uncertainty in θ is generally independent on the number of waterfalls (Figure 6a), and θ is generally insensitive to σ_a (Figure 6b). The θ values do not show a clear covariance with precipitation (Figure 6c). The θ values computed through slope area relations somewhat deviate from those computed based on linear or binning-based optimization of χ-z relations ($\theta_{\chi-z-\mathrm{lin}}$ and $\theta_{\chi-z-\mathrm{bin}}$, respectively, section 2.4 and Figure 7). In some basins the χ-z relations for the flow pathways downslope of the waterfalls are scattered and so are the slope area relations, suggesting that these basins deviate from the linear relation expected when channels are at steady state and lithology and uplift are spatially homogenous (SI).

3.4. Comparison of θ and *p*

Comparison of p and θ shows that they are generally similar within uncertainty (Figure 7 and Tables 1 and S1). The optimal p and θ values generally covary for basins of $\gtrsim$10 waterfalls, Figure 7c). Least squares linear regression between p computed with $A_c = 0$ and θ computed through all the aforementioned methods produces $\theta = 0.054(\pm0.13) + 0.95(\pm0.31)p$ (uncertainty is reported based on 95% confidence interval), with an $R^2 = 0.64$, and a probability value (p-value) of 2.4×10^{-6}. Similar analysis for p computed with $A_c > 0$ produces $\theta = 0.006\,(\pm0.17) + 1.19\,(\pm0.44)\,p$ with an $R^2 = 0.59$ and a probability value (p-value) of 1.2×10^{-5}. Note that in both cases the intercept is <0.1 and the slope is close to unity, suggesting that p and θ

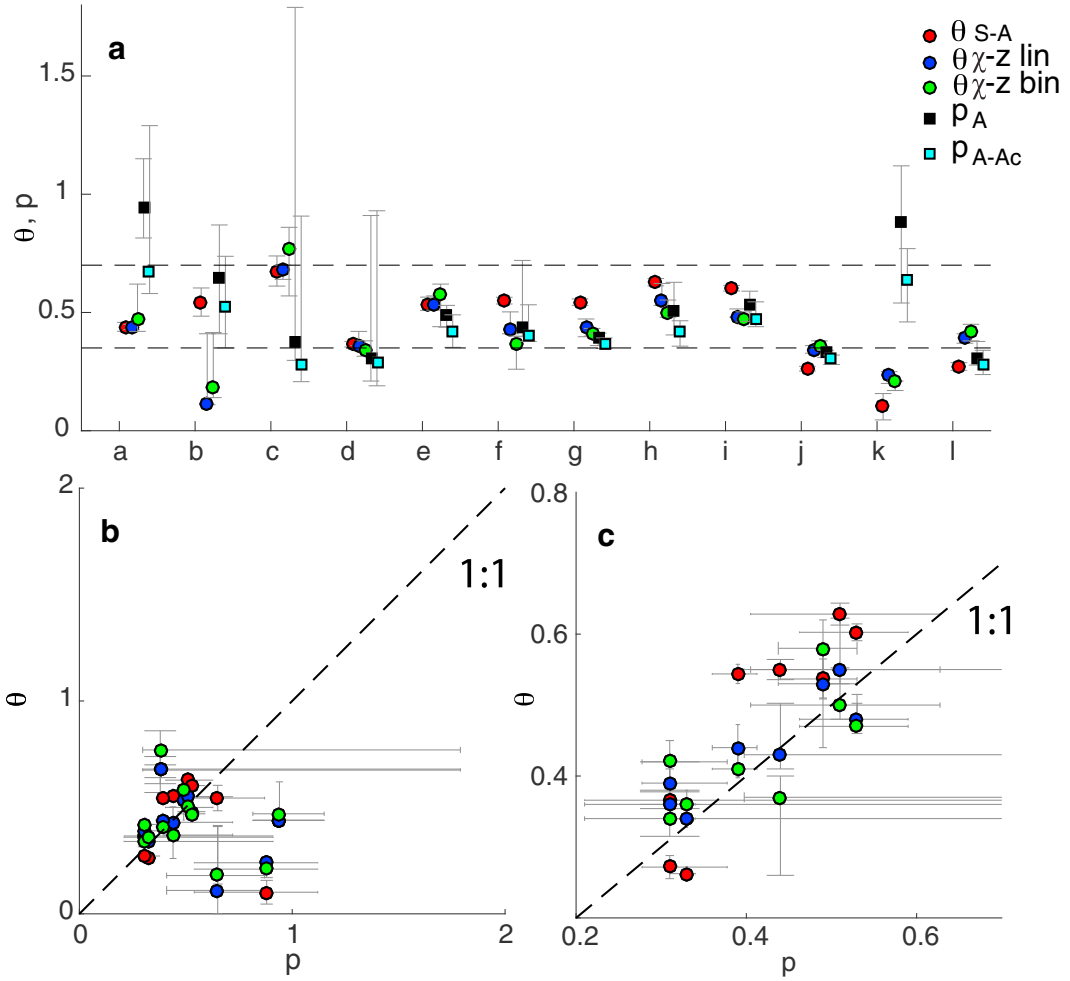

Figure 7. Computed p and θ values. (a) Comparison of p and θ for different basins. The x axis shows the ID of the analyzed basins (in accordance with Table 1), and the y axis shows the value of p and the values of θ for the various methods specified in the figure legend (sections 2.4 and 2.3). The uncertainty values are determined via the procedures described in section 2.5. Note that the uncertainties of p and θ overlap in most cases. The dashed horizontal lines mark the commonly observed θ values (0.35–0.7, (Tucker & Whipple, 2002; Whipple & Tucker, 1999)). (b) A scatter plot of p (x axis) versus θ (y axis) for all basins. The dashed line delineates a 1:1 relations between p and θ. The θ values computed with different methods are colored as in panel a. Note that in many cases the uncertainties of p and θ overlap with this 1:1 line. (c) Same as panel (b), for basins with $\gtrsim 10$ waterfalls. This gives $R^2 = 0.64$ and a probability value (p-value) of 2.4×10^{-6}.

are generally similar. A ranked correlation produces a Kendall correlation coefficient of 0.55 and a probability value p-value of 4.4×10^{-4}. The difference between p and θ is maximal when p values are high (Figure 7a). A Kolmogorov-Smirnov test that compared the distributions of p and θ for all basins failed to reject the null hypotheses that p and θ are drawn from the same population. Similarly, a Wilcoxon signed rank test that compared the paired (by basin) values of p and θ failed to reject the null hypothesis that the population of differences between p and θ pairs comes from a distribution whose median is 0. Note that in both of these tests the null hypothesis (i.e., similarity of p and θ) is not rejected despite the very conservative significance level used ($\alpha = 0.5$, an order of magnitude larger than the commonly used $\alpha = 0.05$).

4. Discussion

4.1. Similarity Between p and θ

The similarity between p and θ is supported through multiple means of comparison. Whereas the similarity "within uncertainty" (Figure 7a) may depend on how the uncertainty in p and θ is computed, the statistical tests are more robust and suggest that the values of p and θ are drawn from the same population (i.e., Kolmogorov-Smirnov test) and that when matched by a basin, neither p or θ is consistently higher than

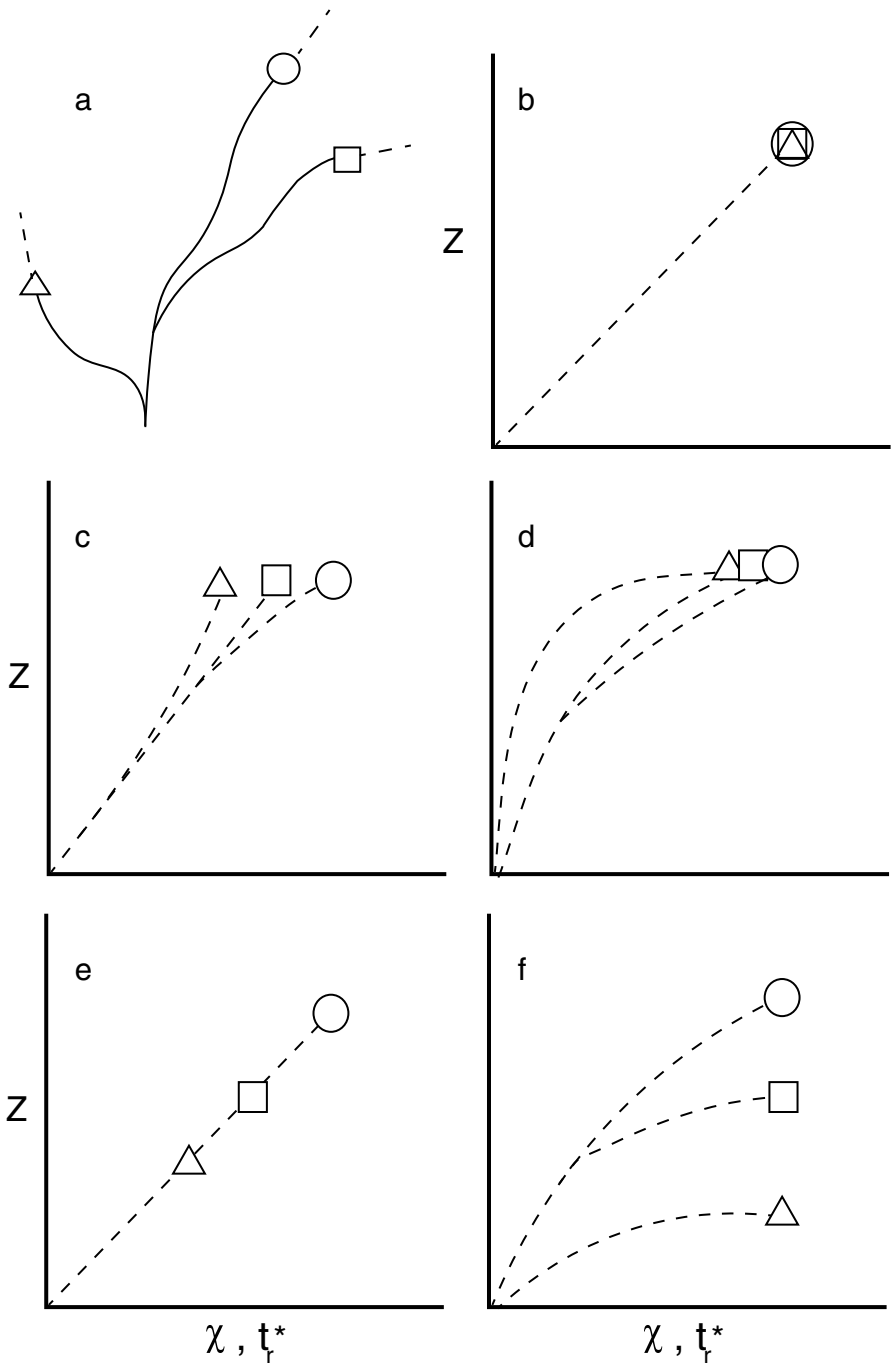

Figure 8. Schematic relations between p and θ in χ-z space. (a) Schematic map of a basin with three waterfalls. Waterfalls are marked with shapes, and the solid and dashed lines mark the channel downstream and upstream of the waterfall, respectively. (b) The χ-z relations when all waterfalls lie at the same elevation and the conditions described in section 2.4.2 are fully satisfied. Here and in the following panels waterfalls are marked by shapes that correspond to those in panel (a), and dashed line marks the χ-z values along the pathway from the origin to the waterfalls. (c) The χ-z relations when waterfalls are at the same elevations, but the conditions in section 2.4.2 are not fully satisfied, and the θ value used to compute χ is that which minimizes the scatter in z for a least square regression between χ and z. (d) The χ-z relations when waterfalls are at the same elevations and the p (or θ) value used to compute the nondimensional recession duration t_r^* (or χ) is that which minimizes the scatter in t_r^* (or χ) for the waterfall locations only. (e) The χ-z relations when waterfalls are at different elevations and the θ value used to compute χ is that which minimizes the scatter in z around a linear regression between χ and z. (f) The χ-z relations when waterfalls are at different elevations and the p (or θ) value used to compute the nondimensional recession duration (t_r^*) is that which minimizes the scatter in t_r^* (or χ) for the waterfall locations only.

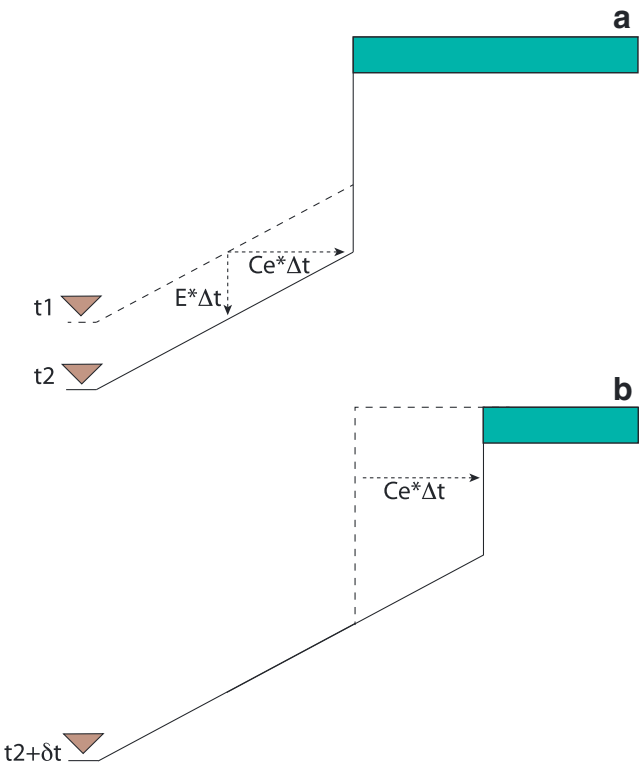

Figure 9. Schematic illustration of a recession mechanism that can cause similarity between the recession of nonvertical channels (C_e) and waterfall recession (C_{ew}) (i.e., $C_e \simeq C_{ew}$) over long time scales (after Haviv et al. (2010)). (a) Channel profile at times t1 (dashed line) and t2 (solid line). Grey triangles represents the base-level elevation at t1 and t2. The Δt is the time span between t1 and t2, such that $E * \Delta t$ is the depth of erosion (E) downstream of the waterfall over this period and $C_e * \Delta t$ is the recession caused by this erosion. In this setting the cap rock layer (colored in green) is resistant to erosion whereas the underlying layers are of higher erodibility. (b) Channel profile following a gravitational collapse of the waterfall and downstream transport of the resulting debris (during a relatively short time period δt). The waterfall at time t2 (dashed line) can collapse through various processes (e.g., undercutting and toppling). Note that in that case the long-term waterfall height is likely set by lithologic properties in conjunction with the gravitational collapse mechanism, and is constant in time and space as long as these properties are constant. Also note that the slope of the channel section downstream of the waterfall is $S = E/C_e$ (see dotted arrows in panel a), such that $C_e = E/S$ and $C_e = KA^mS^n/S = KA^mS^{n-1}$ in the context of the channel incision model.

the other (i.e., Wilcoxon signed rank test). The covariance between p and θ (for basins with 10 waterfalls or more) and their alignment along a ~ 1:1 line further supports their similarity.

One interpretation of the similarity between p and θ is that it stems from the functional similarity between t_r^* and χ (equations (7) and (10)), where both t_r^* and χ at the waterfall can represent the duration of waterfall recession (e.g., Goren et al., 2014; Perron & Royden, 2012; Whipple & Tucker, 1999). Conceptually, when all tributaries collapse to a single line in χ-z space, and the waterfalls are of equal elevation, an equality of p and θ is inevitable (Figures 8a and 8b). However, perfect alignment of χ and z rarely occurs in natural settings, so that different values of p and θ may occur. For example, Figures 8c and 8d show a scenario where waterfalls are of equal elevation but the θ value that minimizes the scatter in z for all χ values along the channels (Figure 8c) differs from the p value that minimizes the scatter in t_r^* at the waterfalls only (Figure 8d). Similarly, Figures 8e and 8f show a scenario with a perfect alignment of χ and z but waterfalls at different elevations, such that once again the θ value that minimizes the scatter in z for all χ values (Figure 8e) differs from the p value that minimizes the scatter in t_r^* at the waterfalls only (Figure 8f). These differences between p and θ occur because p minimizes the scatter in t_r^* (or χ) at the waterfall location only, while θ minimizes the scatter in z for χ (or t_r^*) values everywhere along the analyzed channels.

In most of the analyzed basins waterfalls are approximately at the same elevation (within uncertainty, Figure 3). Whereas this can be interpreted as if the similarity between p and θ stems from the idealized case described in Figure 8b, the lack of clear relations between the spread in waterfall elevations and the difference between p and θ (SI), as well as the scattered χ-z relation for the analyzed basins (SI), suggests that the setting described in Figure 8b is unlikely. Given that the optimization of θ assigns equal weighting to all points along the channel profile and that of p accounts for waterfall location only, the similarity between p and θ may capture commonalities between the processes that shape the channel profile and those that determine the location of waterfalls.

4.2. Potential Process-Based Rationale for the Similarity of p and θ

In the context of the channel incision law, $p = \theta = m/n$ suggests that the exponent value that describes the influence of drainage area (A) on waterfall celerity is similar to that which describes the influence of A on the celerity of nonvertical waterfalls (section 1). This functional similarity may have several explanations.

A potential explanation for $p = m/n$ is that waterfall celerity is primarily influenced by water discharge and channel width, for which $A^{m/n}$ is a proxy (i.e., $m/n = c(1-b)$, where c and b are exponent relating drainage area to channel discharge and width, respectively, Whipple & Tucker, 1999). For example, discharge can influence the retreat of a quasi-vertical waterfall face through plunge pool erosion, by shear on subvertical slabs which will eventually topple, by removing and breaking boulders which can buttress the waterfall face, by supplying sediments that can enhance erosion, and by influencing wet-dry-related weathering of the waterfall face. Since water velocity matters in all these processes, the width of the channel at a given discharge also matters. Hence, waterfall recession may be a function of $A^{m/n}$. Whereas multiple factors influence waterfall celerity (see section 1), many of these factors can covary with channel geometry and discharge and therefore with $A^{m/n}$. Further exploration of the relations between these different factors and $A^{m/n}$ is needed to support this potential explanation and to evaluate the relative influence of processes that do not depend on A on waterfall recession.

An alternate explanation for the similarity between p and m/n is that the recession of a waterfall and that of downstream nonvertical channel segments is dependent. Such dependency was suggested by Haviv et al. (2010), who explored the recession of a waterfall with a resistant cap rock underlain by a weaker sub–cap rock. In that case, Haviv et al. (2010) demonstrated that a recession of a nonvertical channel segment downslope of a waterfall (driven by downstream incision) can result in increased waterfall height once the receding segment abuts against the waterfall (as long as the vertical incision rate below the waterfall is greater than that upstream of the waterfall). When the waterfall height reaches a threshold for gravitationally induced failure, the waterfall fails and recedes, the resulting debris is transported down the channel, and the process repeats (Figure 9).

A mechanism in which the waterfall celerity is dependent on (i.e., enslaved to) the celerity of the downstream channel segment requires that over long time scales the waterfall celerity (C_{ew}) equals the celerity of nonvertical channel segments (C_e). In the context of equations (3)–(5) this requires that the waterfall celerity coefficient (B) equals the channel erodibility K. We are not aware of direct comparisons of these coefficients across basins with well-defined waterfalls such as those explored in this study; however, the B value computed by Berlin and Anderson (2007) for waterfalls in the Roan Plateau, CO ($B = 1.37 \times 10^{-7}$ $[m^{0.08}year]^{-1}$, computed with $p = 0.54$) is within the range of empirically calibrated K values for models with $0.5 \leq m/n \leq 0.59$ and $n = 1$ (Ferrier et al., 2013; Murphy et al., 2016; Stock & Montgomery, 1999). However, a case where waterfall recession is faster than that imposed by channel incision downstream (i.e., $C_{ew} > C_e$) was shown by DiBiase et al. (2015) for the Big Tujunga Creek that is incised into the crystalline rocks of the San-Bernardino mountains, CA. The high recession rate of the Niagara Falls (Gilbert, 1907), for example, is also unlikely to be in balance with the recession imposed by channel incision (i.e., Figure 9) downstream. These examples suggest that the factors that govern waterfall recession may vary in time and space and that a single mechanism is unlikely to explain the variety of observed phenomena. Direct comparison of K, B, p, and θ in locations where erosion rate, as well as the duration and spatial extent of waterfalls retreat are well constrained, can reveal whether, and under what conditions, waterfall recession is enslaved to that of downstream channel segments (Figure 9).

4.3. Examination of Assumptions

The assumption that all waterfalls initiated as a single waterfall at the trunk channel downstream of all waterfalls underlies our computation of p. Whereas we could not test for this assumption, such assumption was previously made for some of the analyzed basins (i.e., Berlin & Anderson, 2007; Weissel & Seidl, 1998) and is common in studies of waterfall and knickpoint propagation (e.g., Brocard et al., 2016; Crosby & Whipple, 2006; DiBiase et al., 2015). The occurrence of waterfalls over a subhorizontal, erosion-resistant layer that is underlain by a weaker layer supports this assumption. This is because it suggests that this layer is initially incised at a downstream location where it is first transected by the stream, and the resulting waterfall then propagates upstream.

A second assumption, which underlies our computation of p, is that the celerity coefficient, B, and the exponent p, are spatially constant along the analyzed channel sections. Spatial homogeneity can stem from the spatial continuity of lithologic layers in many of the analyzed basins. This is suggested by geologic maps (Table 1), air photos, pictures (https://www.google.com/earth/, http://www.panoramio.com), and published work (Berlin & Anderson, 2007; Melis et al., 1996; Ruiz, 2002) that indicate that in most of the analyzed basins the channel system is incised into subhorizontal lithologic layers, and waterfalls occur over spatially continuous erosion-resistant layers underlain by weaker layers (except for basins e–g where this varies spatially [Weissel & Seidl, 1998] and at least some of the waterfalls are composed of a series of small waterfalls). The horizontal continuity of these layers can facilitate spatial homogeneity in B and p, where waterfalls, as well as nonvertical channel segments downstream, everywhere recede over the same lithologic units (e.g., Berlin & Anderson, 2007; Haviv, 2007; Haviv et al., 2006, 2010; Figure 9). Observations concerning the stratigraphic position of waterfalls and whether their lower boundary is tied to a specific lithologic horizon can assist in evaluating the feasibility of stratigraphically controlled homogeneity.

The possibility that the similarity of p and θ stems from enslavement of the waterfall celerity to that of the nonvertical channel downstream of the waterfall is underlain by few assumptions. First, this mechanism was suggested and explored for waterfalls over a resistant cap rock underlaid by a weaker sub–cup rock (Haviv et al., 2010; this also appears to be the case in most of the basins we analyzed) and may not be valid for waterfalls in different settings. Second, in the context of equations (3)–(5) and $p = \theta$ this mechanism requires that downstream channel recession is proportional to $A^{m/n}$, either because $n = 1$ or because at

the downstream channel segment denudation and uplift rates are approximately balanced (i.e., section 1). Such a balance in the downstream channel segment is possible, despite the irregular channel profiles (Figure 3), because of the aforementioned lateral continuity of lithologic layers. In that case, where the spatial homogeneity of θ relies on the lateral continuity of specific layers but the value of θ is computed over the heterogeneous lithology of the entire channel system, it is assumed that this θ value is representative of the value of θ just downstream of the waterfall. In the context of the enslavement mechanism, if the latter assumptions hold so that denudation and uplift are balanced, the similarity between p and θ is not necessarily indicative of $n = 1$.

Finally, the comparison between p and θ and its interpretation from a process perspective assumes that the underlying equations (i.e., equations (2) and (5)) adequately describe the recession process. Whereas both equations were explored numerically and calibrated to field data (e.g., Bishop et al., 2005; Brocard et al., 2016; Crosby & Whipple, 2006; Rosenbloom & Anderson, 1994; Whittaker & Boulton, 2012), alternate or more complicated models can perform equally well or better (e.g., Crosby & Whipple, 2006; Lague, 2014). A wide spread of p values, or a clear indication that an important process is overlooked by equation (5), can raise doubts concerning the validity of this equation. Our results, pointing at a general consistency in the value of p between basins, as well as at a similarity between p and θ, suggest that equations (2) and (5) do capture aspects of the recession process that are consistent across the analyzed basins. This consistency lends some further support to the validity of these equations.

4.4. The Sensitivity of p to Basin Properties and DEM Resolution

The uncertainty in p is sensitive to the number of waterfalls (N_p) within a basin (Figure 5b). In the context of our methodology for computing p, this suggests that when the number of waterfalls is small ($N_p \lesssim 10$, Figure 5b), the influence of each of the flow pathways selected in a bootstrap iteration is large, such that a variety of optimal p values can be produced depending on the selected subset. Our analyses therefore suggest that studies that aim to extract reliable p values with the methodology we used should focus on basins with a large number of waterfalls ($N_p \gtrsim 10$, Figure 5b).

The association between the exceptionally high p value ($p \sim 1$) of basins (a) and (k) ($0.94^{+0.21}_{-0.12}$, $0.88^{+0.24}_{-0.34}$, respectively, for a model with $A_c = 0$), and the low variability in waterfalls drainage area (A_w) that characterize these basins ($\sigma_a \sim 10^6$ m^2, $\sigma_a/\mu_a < 0.5$, Figure 5a), points at a potential dependency between these parameters. Note that basin (d) is associated with a low p value despite a low standard deviation in A_w (σ_a), yet this basin is associated with the lowest mean A_w (μ_a) of all basins ($\sim 2 \times 10^6$ m^2, Table S1), such that its relative standard deviation (i.e., σ_a/μ_a) is higher than that of basins (a) and (k). A dependency between p and the variability in A_w is aligned with the findings of Crosby and Whipple (2006), who computed high p value ($p = 1.125$) for a basin with low variability in A_w .

Occurrence of high p values is predicted for equation (5) when waterfalls drain a similar drainage area (i.e., low variability in A_w, Figures 1 and 5a) but have different distributions of drainage area (A) along the downstream flow pathway. These high p values occur because waterfalls that drain similar drainage areas (i.e., small σ_a) likely have similar A values along the channel just downstream of the waterfall, while further downstream along the waterfall migration pathway (and yet upstream of where flow pathways merge next to the initial waterfall location) values of A differ due to variations in the network topology. In that case, a high p value is preferred by the optimization procedure because it increases the similarity in recession duration (t_r^*) by heavily weighting the low A portion of the channel just downstream of the waterfall where the values of A are similar among channels (i.e., equation (7)). As σ_a increases, lower p values are favored because they preferably weight the identical high A portion of channels downstream of large confluences where channels merge. This topologic argument suggests that high p values will be associated with relatively low values of σ_a.

To explore this prediction, we run multiple p optimization experiments where we used the topology (i.e., drainage area as a function of distance along the channels) for basin (g) and imposed randomly positioned waterfalls within this basin topology. An initial set of N_{s1} waterfall locations, constrained by a prescribed range of drainage area, was randomly selected from all possible locations for basin (g). From this initial set we excluded all waterfall locations that have other waterfalls draining to them. From this screened subset of random locations we then randomly selected a prescribed number of waterfalls (N_{s2}) and used it to optimize p. To test the sensitivity of p to σ_a in this synthetic situation, the dependent variable was σ_a, namely, the permissible range of drainage areas from which the N_{s1} locations are selected while maintaining the mean value of A_w

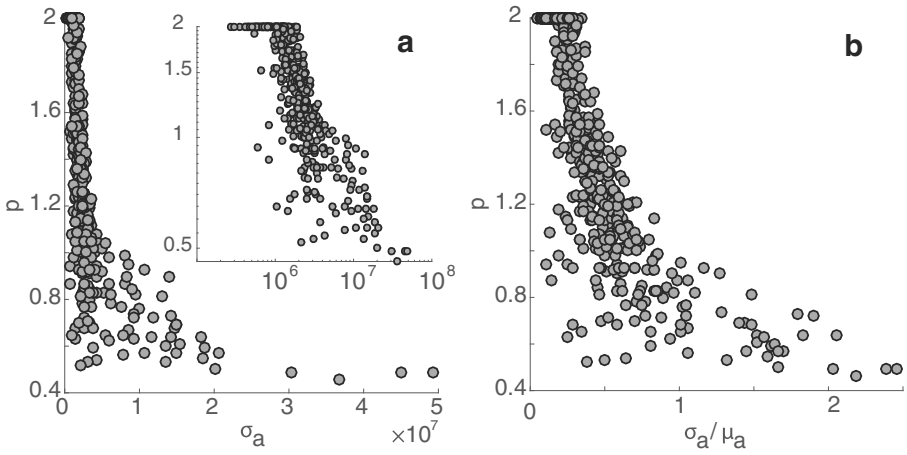

Figure 10. Relations between p and σ_a for experiments with arbitrary waterfalls positioned in basin (g) plotted in linear (a) and logarithmic (inset of panel a) scales. Each filled circle shows the values of p and σ_a for a single experiment with 11 waterfalls that are arbitrary positioned. (b) p versus the relative standard deviation in A_w (σ_a/μ_a).

(μ_a) approximately the same. We conducted 500 experiments with arbitrarily located waterfalls ($N_{s1} = 20$ and $N_{s2} = 11$). In each experiment we recorded the standard deviation of A_w (σ_a), as well as the relative standard deviation (σ_a/μ_a) and optimal p value. The results of this experiment show that a high value of p is indeed associated with low σ_a. As σ_a increases, the value of p first declines steeply and then more gradually reaching approximately $p = 0.5$ at higher σ_a values (Figure 10).

The interpretation of p values computed for low σ_a should also account for the potential influence of DEM resolution. For example, waterfalls within the same basin may retreat according to equation (5) with a p value of 0.5 up to the upper reaches of the basin, where the area that drains to waterfalls (A_w) decreases and so does the waterfall celerity. When mapped over a low-resolution DEM, all waterfalls may appear to have the same A_w so the optimization procedure will prefer a higher value of p. In contrast, when mapped over high-resolution DEM, small differences in A_w will become apparent so $p = 0.5$ can be recovered. Hence, DEMs of higher resolution will allow more accurate recovery of p, and for a given resolution, p values computed for basins with high σ_a are likely more reliable.

For high values of σ_a the optimal p value for the synthetic experiments with arbitrary waterfall locations is in the range that is typical of θ (Figure 10). This can be interpreted as if the similarity between p and θ is insensitive to the exact location of waterfalls and that p can be predicted from σ_a (SI). However, the covariance between p and θ for basins of $\geq$ 10 waterfalls (Figure 7c), together with the low covariance between θ and σ_a (Figure 6c), suggests that the natural location of waterfalls is associated with significant subtleties in the value of p that reflect differences in the underlying process.

5. Summary

This study explores the similarity between channel profile concavity (i.e., the exponent θ) downstream of waterfalls and the exponent p that is used to model waterfall recession. We analyzed channel profiles and the locations of waterfalls at 12 basins with different climatic and lithologic conditions and also developed a new method to compute the optimal value of p and its uncertainty. Our results demonstrate that the values of p and θ are similar within uncertainty, come from a similar population, and generally covary for basins with $\gtrsim$10 waterfalls. In the context of the channel incision models this suggests that in the basins we analyzed waterfall recession is influenced by channel discharge and width as approximated by $A^{m/n}$ and/or that the waterfall celerity is enslaved to that of downstream channel segments.

Deviations between p and θ primarily arise when p values are relatively high due to low variability in the area that drains to waterfalls or to high uncertainty in p. This may occur when waterfall recession decreases at low A values and the DEM resolution is relatively low, or when the number of waterfalls in a basin is >10. To avoid

these influences, we recommend that p values be computed over basins with a relatively large spread in A_w (i.e., $\sigma_a/\mu_a > 1$) and large number of waterfalls (>10).

Future studies focused on the relations between the waterfall celerity coefficient (B), and the channel erodibility coefficient (K) may reveal whether, and for what conditions, waterfall celerity is similar to that of nonvertical channel segments. Such similarity would suggest that waterfall recession is enslaved to that of downstream segments. Furthermore, similarity would mean that landscape evolution models that implement the stream power or shear stress incision models are also suitable for simulating landscape evolution in the presence of waterfalls.

Notation

A drainage area [L^2]
A_0 reference drainage area [L^2]
A_c critical drainage area threshold [L^2]
A_i drainage area at a node i [L^2]
A_w area that drains to a waterfall [L^2]
A_r normalized drainage area used for plotting []
B waterfall celerity coefficient [L^{1-2p}/T]
b exponent that relates drainage area to channel width []
C_e knickpoint celerity [L/T]
C_{eW} waterfall celerity [L/T]
$C_{ew,i}$ the waterfall celerity between nodes i and $i+1$ [L/T]
c exponent that relates drainage area to channel discharge []
D_i measure of difference used in computing χ_r^2, units vary with model
E erosion rate [L/T]
i index of nodes []
K erodibility coefficient in channel incision law [L^{1-2m}/T]
k_s channel steepness [$L^{2m/n}$]
k_{sn} normalized channel steepness [$L^{2m/n}$]
k_{sn_i} normalized channel steepness at a node i [$L^{2m/n}$]
l along stream flow distance up flow from l_b [L]
l_b along stream flow distance up flow from an arbitrary location [L]
m drainage area exponent in channel incision model []
N_n number of nodes between the initial waterfall location at t_s and some upstream node []
N_p number of data points used in computing χ_r^2 []
N_{s1} number of potential waterfall locations in a random selection process []
N_{s2} number of waterfalls selected from a subset of randomly positioned waterfalls that do not drain to each other []
n slope exponent in channel incision model []
p drainage area exponent in posited waterfall celerity model []
S channel slope []
S_i slope at a node i []
t_r duration of waterfall recession [T]
t_r^* nondimensional duration of waterfall recession []
$\bar{t}_r^*$ mean nondimensional duration of waterfall recession for all waterfalls in a basin[]
t_s time of initial waterfall formation [T]
U uplift rate [L/T]
U_n new uplift rate that is higher than the initial one[L/T]
z elevation [L]
z_i elevation at a node i [L]
α statistical significance level []
δ_i dimensionless variable that equals 1 or $\sqrt{2}$ for cardinal and diagonal flow direction between nodes i and $i+1$, respectively []
δt small time increment [T]
Δt_0 reference waterfall recession duration [T]

Δt_i recession duration between nodes i and $i+1$ [T]
Δt_i^* nondimensional waterfall recession duration []
Δx distance between DEM nodes in the cardinal directions [L]
μ_a mean of A_w in a basin [L^2]
μ_z mean of waterfall elevation in a basin [L]
θ the ratio between the exponents m and n in the channel incision model []
θ_{SA} the value of θ computed from the log(A) versus log(S) []
$\theta_{\chi-z}$ the value of θ computed from χ-z relations []
$\theta_{\chi-z-lin}$ the value of θ computed from linear χ-z relations []
$\theta_{\chi-z-bin}$ the value of θ computed from binned χ-z relations []
σ_i measure of uncertainty used in computing χ_r^2, units vary with model
σ_a standard deviation of A_w in a basin [L^2]
σ_z standard deviation of waterfall elevation in a basin [L]
Σ_z vertical uncertainty in DEM [L]
χ transformation variable that links channel drainage area and length to elevation [L]
χ_r^2 measure of weighted misfit in recession duration [].

Acknowledgments
Data supporting our analysis is contained as tables and figures within the manuscript and supporting information. Relevant code is available at http://www.pitt.edu/~shelef/. We thank Joel Johnson and two anonymous reviewers for constructive and insightful comments that helped improve this manuscript. We are particularly thankful to Joel Scheingross for insightful and thorough review. E. S. thanks S. Willett and S. Gallen for constructive discussions regarding the impact of waterfalls on landscape evolution.

References

Bagnold, R. (1966). An approach to the sediment transport problem from general physics (U.S. Geological Survey Professional Paper 422-1.) Washington, DC: US Government Printing Office.

Berlin, M. M., & Anderson, R. S. (2007). Modeling of knickpoint retreat on the Roan Plateau, western Colorado. *Journal of Geophysical Research*, *112*, F03S06. https://doi.org/10.1029/2006JF000553

Bishop, P., Hoey, T. B., Jansen, J. D., & Artza, I. L. (2005). Knickpoint recession rate and catchment area: The case of uplifted rivers in Eastern Scotland. *Earth Surface Processes and Landforms*, *30*(6), 767–778. https://doi.org/10.1002/esp.1191

Brocard, G. Y., Willenbring, J. K., Miller, T. E., & Scatena, F. N. (2016). Relict landscape resistance to dissection by upstream migrating knickpoints. *Journal of Geophysical Research: Earth Surface*, *121*, 1182–1203. https://doi.org/10.1002/2015JF003678

Crosby, B. T., & Whipple, K. X. (2006). Knickpoint initiation and distribution within fluvial networks: 236 waterfalls in the Waipaoa River, North Island, New Zealand. *Geomorphology*, *82*(1), 16–38. https://doi.org/10.1016/j.geomorph. 2005.08.023

DiBiase, R. A., Whipple, K. X., Lamb, M. P., & Heimsath, A. M. (2015). The role of waterfalls and knickzones in controlling the style and pace of landscape adjustment in the western San Gabriel Mountains, California. *Geological Society of America Bulletin*, *127*(3-4), 539–559. https://doi.org/10.1130/B31113.1

Dietrich, W. E., Bellugi, D. G., Sklar, L. S., Stock, J. D., Heimsath, A. M., & Roering, J. J. (2003). Geomorphic transport laws for predicting landscape form and dynamics. In P. Wilcock & R. Iverson (Eds.), *Prediction in geomorphology, Geophysical Monograph Series* (Vol. 135, pp. 103–132). American Geophysical Union: Washington, DC: American Geophysical Union. https://doi.org/10.1029/135GM09

Ferrier, K. L., Huppert, K. L., & Perron, J. T. (2013). Climatic control of bedrock river incision. *Nature*, *496*(7444), 206–209. https://doi.org/10.1038/nature11982

Gasparini, N. M., Bras, R. L., & Whipple, K. X. (2006). Numerical modeling of non–steady-state river profile evolution using a sediment-flux-dependent incision model. In S. D. Willett, et al. (Eds.), *Tectonics, climate, and landscape evolution. Geological Society of America Special Paper*, *398*, (127–141). https://doi.org/10.1130/2006.2398(04)

Gilbert, G. K. (1907). Rate of recession of Niagara Falls. *U.S. Geological Survey Bulletin*, *306*, 1–31.

Goren, L. (2016). A theoretical model for fluvial channel response time during time-dependent climatic and tectonic forcing and its inverse applications. *Geophysical Research Letters*, *43*, 10–753. https://doi.org/10.1002/2016GL070451

Goren, L., Fox, M., & Willett, S. D. (2014). Tectonics from fluvial topography using formal linear inversion: Theory and applications to the Inyo Mountains, California. *Journal of Geophysical Research: Earth Surface*, *119*, 1651–1681. https://doi.org/10.1002/2014JF003079

Hack, J. T. (1973). Stream-profile analysis and stream-gradient index. *Journal of Research of the US Geological Survey*, *1*(4), 421–429.

Hail, W. J. (1992). Geology of the central Roan Plateau area, northwestern Colorado. *U.S. Geological Survey Bulletin*, *1787-R*, 26.

Haviv, I. (2007). Mechanics, morphology and evolution of vertical knickpoints (waterfalls) along the bedrock channels of the Dead Sea western tectonic escarpment (PhD thesis). Hebrew University of Jerusalem, Israel.

Haviv, I., Enzel, Y., Whipple, K., Zilberman, E., Matmon, A., Stone, J., & Fifield, K. (2010). Evolution of vertical knickpoints (waterfalls) with resistant caprock: Insights from numerical modeling. *Journal of Geophysical Research*, *115*, F03028. https://doi.org/10.1029/2008JF001187

Haviv, I., Enzel, Y., Whipple, K., Zilberman, E., Stone, J., Matmon, A., & Fifield, L. (2006). Amplified erosion above waterfalls and oversteepened bedrock reaches. *Journal of Geophysical Research*, *111*, F04004. https://doi.org/10.1029/2006JF000461

Howard, A. D., & Kerby, G. (1983). Channel changes in badlands. *Geological Society of America Bulletin*, *94*(6), 739–752. https://doi.org/10.1130/0016-7606(1983)943C739:CCIB3E2.0.CO;2

Howard, A. D., & Kochel, R. (1988). Introduction to cuesta landforms and sapping processes on the Colorado Plateau. In *Sapping features of the Colorado Plateau: A comparative planetary geology field guide* (Vol. 491, pp. 6). Springfield, VA: Scientific and Technical Information Office, National Aeronautics and Space Administration.

Lague, D. (2014). The stream power river incision model: Evidence, theory and beyond. *Earth Surface Processes and Landforms*, *39*(1), 38–61. https://doi.org/10.1002/esp.3462

Lamb, M. P., Howard, A. D., Johnson, J., Whipple, K. X., Dietrich, W. E., & Perron, J. T. (2006). Can springs cut canyons into rock? *Journal of Geophysical Research*, *111*, E07002. https://doi.org/10.1029/2005JE002663

Lamb, M. P., Howard, A. D., Dietrich, W. E., & Perron, J. T. (2007). Formation of amphitheater-headed valleys by waterfall erosion after large-scale slumping on Hawaii. *Geological Society of America Bulletin*, *119*(7-8), 805–822. https://doi.org/10.1130/B25986.1

Lamb, M. P., Mackey, B. H., & Farley, K. A. (2014). Amphitheater-headed canyons formed by megaflooding at Malad Gorge, Idaho. *Proceedings of the National Academy of Sciences of the United States of America*, *111*(1), 57–62. https://doi.org/10.1073/pnas.1312251111

Mackey, B. H., Scheingross, J. S., Lamb, M. P., & Farley, K. A. (2014). Knickpoint formation, rapid propagation, and landscape response following coastal cliff retreat at the last interglacial sea-level highstand: Kaua'i, Hawai'i. *Geological Society of America Bulletin*, *126*(7-8), 925–942. https://doi.org/10.1130/B30930.1

Mason, P. J., & Arumugam, K. (1985). Free jet scour below dams and flip buckets. *Journal of Hydraulic Engineering*, *111*(2), 220–235.

Melis, T. S., Phillips, W. M., Webb, R. H., & Bills, D. J. (1996). When the blue-green waters turn red: Historical flooding in Havasu Creek, Arizona (US Geological Survey water-resources investigations report 96–4059). Tucson, AZ.

Montgomery, D. C., & Runger, G. C. (2010). *Applied statistics and probability for engineers*. New York: John Wiley.

Montgomery, D. R., & Buffington, J. M. (1997). Channel-reach morphology in mountain drainage basins. *Geological Society of America Bulletin*, *109*(5), 596–611. https://doi.org/10.1130/0016-7606(1997)109<0596:CRMIMD>2.3.CO;2

Montgomery, D. R., Buffington, J. M., Smith, R. D., Schmidt, K. M., & Pess, G. (1995). Pool spacing in forest channels. *Water Resources Research*, *31*(4), 1097–1105. https://doi.org/10.1029/94WR03285

Moon, S., Chamberlain, C. P., Blisniuk, K., Levine, N., Rood, D. H., & Hilley, G. E. (2011). Climatic control of denudation in the deglaciated landscape of the Washington Cascades. *Nature Geoscience*, *4*(7), 469–473. https://doi.org/10.1038/ngeo1159

Mudd, S. M., Attal, M., Milodowski, D. T., Grieve, S. W., & Valters, D. A. (2014). A statistical framework to quantify spatial variation in channel gradients using the integral method of channel profile analysis. *Journal of Geophysical Research: Earth Surface*, *119*, 138–152. https://doi.org/10.1002/2013JF002981

Murphy, B. P., Johnson, J. P., Gasparini, N. M., & Sklar, L. S. (2016). Chemical weathering as a mechanism for the climatic control of bedrock river incision. *Nature*, *532*(7598), 223–227. https://doi.org/10.1038/nature17449

Niemann, J. D., Gasparini, N. M., Tucker, G. E., & Bras, R. L. (2001). A quantitative evaluation of Playfair's law and its use in testing long-term stream erosion models. *Earth Surface Processes and Landforms*, *26*(12), 1317–1332. https://doi.org/10.1002/esp.272

Perron, J. T., & Royden, L. (2012). An integral approach to bedrock river profile analysis. *Earth Surface Processes and Landforms*, *38*, 570–576. https://doi.org/10.1002/esp.3302

Rodríguez, E., Morris, C., Belz, J., Chapin, E., Martin, J., Daffer, W., & Hensley, S. (2005). An assessment of the SRTM topographic products (Tech. Rep., JPL D-31639). Pasadena, CA: Jet Propulsion Laboratory.

Rosenbloom, N. A., & Anderson, R. S. (1994). Hillslope and channel evolution in a marine terraced landscape, Santa Cruz, California. *Journal of Geophysical Research*, *99*(B7), 14,013–14,029. https://doi.org/10.1029/94JB00048

Royden, L., & Perron, T. J. (2013). Solutions of the stream power equation and application to the evolution of river longitudinal profiles. *Journal of Geophysical Research: Earth Surface*, *118*, 497–518. https://doi.org/10.1002/jgrf.20031

Royden, L., Clark, M., & Whipple, K. (2000). Evolution of river elevation profiles by bedrock incision: Analytical solutions for transient river profiles related to changing uplift and precipitation rates. *Eos, Transactions American Geophysical Union*, *81*, 48.

Ruiz, G. M. H. (2002). Exhumation of the northern Sub-Andean Zone of Ecuador and its source regions (PhD thesis, Diss.). Naturwissenschaften ETH Zürich, Nr. 14905, 2003.

Scheingross, J. S., & Lamb, M. P. (2016). Sediment transport through self-adjusting, bedrock-walled waterfall plunge pools. *Journal of Geophysical Research: Earth Surface*, *121*, 939–963. https://doi.org/10.1002/2015JF003620

Scheingross, J. S., Lo, D. Y., & Lamb, M. P. (2017). Self-formed waterfall plunge pools in homogeneous rock. *Geophysical Research Letters*, *44*, 200–208. https://doi.org/10.1002/2016GL071730

Seidl, M., & Dietrich, W. (1992). The problem of channel erosion into bedrock. In K. Schmidt & J. de Ploey (Eds.), *Functional geomorphology: Landform analysis and models: Festschrift for Frank Ahnert* (Vol. Catena Supplement 23, pp. 101–124). Cremlingen, Germany: Catena Verlag.

Seidl, M. A., Weissel, J. K., & Pratson, L. F. (1996). The kinematics and pattern of escarpment retreat across the rifted continental margin of SE Australia. *Basin Research*, *8*(3), 301– 316.

Shelef, E., & Hilley, G. E. (2014). Symmetry, randomness, and process in the structure of branched channel networks. *Geophysical Research Letters*, *41*, 3485–3493. https://doi.org/10.1002/2014GL059816

Stock, J. D., & Montgomery, D. R. (1999). Geologic constraints on bedrock river incision using the stream power law. *Journal of Geophysical Research*, *104*, 4983–4993. https://doi.org/10.1029/98JB0213

Tucker, G., & Hancock, G. (2010). Modeling landscape evolution. *Earth Surface Processes and Landforms*, *35*(1), 28–50. https://doi.org/10.1002/esp.1952

Tucker, G., & Whipple, K. (2002). Topographic outcomes predicted by stream erosion models: Sensitivity analysis and intermodel comparison. *Journal of Geophysical Research*, *107*(B9), 2179. https://doi.org/10.1029/2001JB000162

Weissel, J. K., & Seidl, M. A. (1997). Influence of rock strength properties on escarpment retreat across passive continental margins. *Geology*, *25*(7), 631–634. https://doi.org/10.1130/0091-7613(1997)025<0631:IORSPO>2.3.CO;2

Weissel, J. K., & Seidl, M. A. (1998). Inland propagation of erosional escarpments and river profile evolution across the southeast Australian passive continental margin. In *Rivers over rock: fluvial processes in bedrock channels* (Vol. 107, pp. 189–206). Washington, DC: American Geophysical Union.

Whipple, K., & Tucker, G. (1999). Dynamics of the stream-power river incision model: Implications for height limits of mountain ranges, landscape response timescales, and research needs. *Journal of Geophysical Research*, *104*, 17,661–17,674. https://doi.org/10.1029/1999JB900120

Whittaker, A. C., & Boulton, S. J. (2012). Tectonic and climatic controls on knickpoint retreat rates and landscape response times. *Journal of Geophysical Research*, *117*, F02024. https://doi.org/10.1029/2011JF002157

Willett, S. D., McCoy, S. W., Perron, J. T., Goren, L., & Chen, C.-Y. (2014). Dynamic reorganization of river basins. *Science*, *343*(6175), 1248765. https://doi.org/10.1126/science.1248765

Wobus, C., Whipple, K. X., Kirby, E., Snyder, N., Johnson, J., Spyropolou, K., et al. (2006). Tectonics from topography: Procedures, promise, and pitfalls. *Geological Society of America Special Papers*, *398*, 55–74. https://doi.org/10.1130/2006.2398(04)

Wobus, C. W., Crosby, B. T., & Whipple, K. X. (2006). Hanging valleys in fluvial systems: Controls on occurrence and implications for landscape evolution. *Journal of Geophysical Research*, *111*, F02017. https://doi.org/10.1029/2005JF000406

Zaprowski, B. J., Pazzaglia, F. J., & Evenson, E. B. (2005). Climatic influences on profile concavity and river incision. *Journal of Geophysical Research*, *110*, F03004. https://doi.org/10.1029/2004JF000138